Posted: November 5, 2019

Extracting elastic constitutive parameters using the VFM within peridynamics

Rolland Delorme[1,*], Patrick Diehl[1], Ilyass Tabiai[1], Louis Laberge Lebel[2], and Martin Lévesque[1]

[1]Laboratory for Multiscale Mechanics, Polytechnique Montreal
[2]Advanced Composite and Fiber Structures Laboratory, Polytechnique Montreal
[*]Corresponding author: ORCID: https://orcid.org/0000-0001-7637-3936

Abstract

This paper implements the Virtual Fields Method within the ordinary state based peridynamic framework to identify material properties. The key equations derived in this approach are based on the principle of virtual works written under the ordinary state based peridynamic formalism for two-dimensional isotropic linear elasticity. In-house codes including a minimization process have also been developed to implement the method. A three-point bending test and two independent virtual fields arbitrarily chosen are used as a case study throughout the paper. The numerical validation of the virtual fields method has been performed on the case study by simulating the displacement field by finite element analysis. This field has been used to extract the elastic material properties and compared them to those used as input in the finite element model, showing the robustness of the approach. Noise analysis and the effect of the missing displacement fields on the specimen's edges to simulate digital image correlation limitations have also been studied in the numerical part. This work focuses on pre-damage properties to demonstrate the feasibility of the method and provides a new tool for using full-field measurements within peridynamics with a reduced calculation time as there is no need to compute the displacement field. Future works will deal with damage properties which is the main strength of peridynamics.

Nomenclature

Material properties

E	Young's modulus [MPa]
ν	Poisson's ratio
K	Bulk modulus [MPa]
G	Shear modulus [MPa]

Geometrical parameters

h	Mesh size / Nodal spacing [mm]
L	Length of the beam [mm]
S	Distance between the pins to supporting pins [mm]
S_f	Surface with prescribed loading [mm^2]
S_u	Surface with prescribed displacement [mm^2]
t	Thickness [mm]
V_f	Volume with prescribed loading [mm^3]
V_u	Volume with prescribed displacement [mm^3]
W	Width of the beam [mm]

Classical continuum mechanics tensors

$\boldsymbol{\sigma}$	Cauchy stress tensor [Components in MPa]
$\boldsymbol{\varepsilon}$	Infinitesimal strain tensor
$\widehat{\boldsymbol{\varepsilon}}$	Actual infinitesimal strain tensor
$\boldsymbol{\varepsilon}^\star$	Virtual infinitesimal strain tensor
$\mathbf{C}$	Stiffness tensor [Components in MPa]

Peridynamic objects

δ	Peridynamic horizon [mm]
$\mathcal{H}$	Family of a material point
$\mathcal{H}_i$	Discrete family of a node i
$\mathcal{H}_{\boldsymbol{x}}$	Spherical region centered on $\boldsymbol{x}$
q	Peridynamic weighted volume
$\boldsymbol{\xi}$	Peridynamic bond
$\boldsymbol{f_v}$	Dual force density [Components in N mm^{-6}]
$\boldsymbol{t_v}$	Bond force density [Components in N mm^{-6}]
$\underline{\mathbf{M}}$	Deformed direction state
$\underline{\mathbf{T}}$	Force state [Components in N mm^{-6}]
$\underline{\mathbf{Y}}$	Deformation state [Components in mm]
$\underline{w}$	Influence state
$\underline{e}^s$	Spherical extension state [Magnitude in mm]
$\underline{e}^d$	Deviatoric extension state [Magnitude in mm]
α^s	Spherical peridynamic parameter
α^d	Deviatoric peridynamic parameter

Position and displacement vectors

$\boldsymbol{x}$	Reference position vector [Components in mm]
$\boldsymbol{y}$	Deformed position vector [Components in mm]
$\boldsymbol{u}$	Displacement vector [Components in mm]
$\overline{\boldsymbol{u}}$	Prescribed displacement vector [Components in mm]
$\widehat{\boldsymbol{u}}$	Actual displacement vector [Components in mm]
$\boldsymbol{u}^\star$	Virtual displacement vector [Components in mm]

Force vectors

$\boldsymbol{b}$	Body force density vector [Components in N mm^{-3}]
$\boldsymbol{F}$	Force vector [Components in N]
$\overline{\boldsymbol{F}}$	Prescribed force vector [Components in N]
$\overline{\boldsymbol{T}}$	Prescribed surface force vector [Components in N mm^{-2}]

Other Symbols

I	Search interval
$\mathcal{C}$	Set of kinematically admissible displacement fields
$\mathcal{S}$	Set of statically admissible displacement fields
$W_{int}^\star$	Internal virtual work within classical continuum mechanics [N mm]
$W_{ext}^\star$	External virtual work within classical continuum mechanics [N mm]
$\mathcal{W}_{int}^\star$	Internal virtual work within peridynamics [N mm]
$\mathcal{W}_{ext}^\star$	External virtual work within peridynamics [N mm]
ϵ	Tolerance to end the minimization process
ϵ_K	Relative error related on the bulk modulus
ϵ_G	Relative error related on the shear modulus
μ	Mean of a Gaussian distribution
Φ	Residual function to minimize in the virtual field method
Σ	Standard deviation of a Gaussian distribution
Ω	Domain of an elastic body
Ω_0	Domain of an elastic body in the reference configuration

1 Introduction

Peridynamics (PD) reformulates continuum mechanics balance laws [Silling, 2000] through the non-local integration of the interactions between material points. Each material point interacts with its neighbors within a finite δ-radius region, the so-called *horizon*. Contrary to classical continuum mechanics, the PD governing equations are directly expressed in terms of force and displacement between material points, instead of spatial derivatives. This makes PD a suitable framework to address discontinuities, like cracks occurring in damage process [Silling, 2016]. Moreover, crack initiation and growth are addressed with only a single critical damage parameter that is triggered when a threshold is reached. This threshold can for example be related to the well-known free energy release rate [Silling and Askari, 2005, Foster et al., 2011] or to the J-integral value [Silling and Lehoucq, 2010]. Therefore, the cracks propagate autonomously within the PD framework and no predefined path, nor other external criteria are needed. Different fracture modes can therefore be accounted for [Hu et al., 2015]. Extended finite elements, cohesive zone models and PD predictions are compared against experimental data [Agwai et al., 2010] for crack initiation and growth. The authors found that PD yields the more natural crack path, including branching and micro-branching.

Many authors have attempted to clarify the horizon concept [Bobaru et al., 2009, Bobaru and Hu, 2012] since this is a major PD parameter. In addition, well-known and accepted constitutive theories and methods derived within classical continuum mechanics have yet to be transposed into the PD framework [Bobaru et al., 2016, Delorme et al., 2017].

Full-field measurements can be used to obtain every material parameter from a single, heterogeneous, mechanical test [Avril and Pierron, 2007]. Full displacement fields can be obtained with surface measurements techniques like Digital Image Correlation (DIC). Finite Element Model Updating Method [Cottin et al., 1984, Rouger et al., 1991, Lecompte et al., 2007], the Constitutive Equation Gap Method [Florentin and Lubineau, 2010], the Equilibrium Gap Method [Claire et al., 2004] or the Virtual Fields Method [Pierron and Grédiac, 2012] have been developed within classical continuum mechanics to obtain material parameters from such full-field measurements. These methods were also described in terms of flexibility of use, full-field displacement data accuracy, noise sensibility, computation time, etc. [Avril et al., 2008].

To the best of the authors' knowledge, only a handful of publications focused on full-field measurements and inverse methods to identify constitutive parameters within PD. An approach which combines DIC and PD was developed [Turner, 2014] to determine full-field displacements for problems involving discontinuities. The principle is to use DIC where it is accurate, *i.e.* in continuous zones, and to add PD calculations in discontinuous regions. Thus, the full-field displacement solution is the combination of the DIC and PD calculations. An inverse method within state-based PD and using a Tikhonov regularization was developed [Turner et al., 2015] to extract the material properties and it provides promising prospects for damage characterization. However, it requires to compute the displacement field from the PD model at each step, which can be time consuming. Also, the robustness of the method against the initial guesses feeded in the minimization objective function and the selection or the effect of the horizon on the convergence were not studied.

The purpose of this work is to derive an equivalence to the Virtual Fields Method (VFM) within the PD framework to identify material properties. A key point of the VFM, when compared to the other methods, is that no computation of the displacement field during the optimization process is needed. Moreover, this work focuses on pre-damage properties to demonstrate the feasibility of the Peridynamics-Virtual Fields Method (PD-VFM).

The paper is organized as follows. Sec. 2 recalls background information about the VFM within classical continuum mechanics and the PD framework. Sec. 3 explains the VFM using the theorem of virtual works formulated within the state-based PD framework. Sec. 4 presents a three-point bending simulation which is the case study used in the sequel. Sec. 5 describes the numerical implementation of the PD-VFM. Finally, Sec. 6 provides a numerical validation in which the displacement field of a three-point bending test has been simulated by finite element analysis and used to extract the material properties which have been then compared to those used as model input. The following notation is adopted in the paper:

- Light-faced letters (*e.g.* a, α, A) denote constants or scalar quantities;
- Bold-faced roman letters (*e.g.* $\boldsymbol{a}$, $\boldsymbol{A}$) denote first-order tensors;
- Bold-faced lowercase greek letters (*e.g.* $\boldsymbol{\alpha}$) denote second-order tensors;
- Non-italic bold-faced capital roman letters (*e.g.* $\mathbf{A}$) denote fourth-order tensors;

- Underlined light-faced lowercase letters (*e.g.* $\underline{a}$) denote scalar states;
- Underlined bold-faced capital letters (*e.g.* $\underline{\mathbf{A}}$) denote vector states;
- "$\otimes$" is the tensor product and ":" is the doubly contracted product;
- Index notation and Einstein summation convention are used, unless specified otherwise.

2 Background

2.1 Virtual Fields Method (VFM) within classical continuum mechanics

2.1.1 Fundamental equations

Consider an elastic body within a domain Ω bounded by $\partial\Omega$ and governed by the following equations:

The equilibrium equation, assuming long-range forces are negligible

$$\begin{cases} \nabla \cdot \boldsymbol{\sigma} = \mathbf{0} \text{ in } \Omega & \text{(1a)} \\ \boldsymbol{\sigma} \cdot \boldsymbol{n} = \overline{\boldsymbol{T}} \text{ on } S_f \subset \partial\Omega & \text{(1b)} \end{cases}$$

where $\boldsymbol{\sigma}$ is the Cauchy stress tensor, $\boldsymbol{n}$ the outward unit normal vector and $\overline{\boldsymbol{T}}$ the prescribed load acting on the surfaces S_f.

The kinematic compatibility equation, within the infinitesimal strain theory

$$\begin{cases} \boldsymbol{\varepsilon} = \dfrac{1}{2}\left(\nabla \cdot \boldsymbol{u} + \nabla^t \cdot \boldsymbol{u}\right) \text{ in } \Omega & \text{(2a)} \\ \boldsymbol{u} = \overline{\boldsymbol{u}} \text{ on } S_u \subset \partial\Omega & \text{(2b)} \end{cases}$$

where $\boldsymbol{\varepsilon}$ is the strain tensor, $\boldsymbol{u}$ the displacement vector and $\overline{\boldsymbol{u}}$ the prescribed displacement acting on the surface S_u. S_f and S_u are such as $S_f \cup S_u = \partial\Omega$ and $S_f \cap S_u = \emptyset$.

The constitutive equation

$$\begin{cases} \boldsymbol{\sigma} = \mathbf{C} : \boldsymbol{\varepsilon} \text{ in } \Omega & \text{(3a)} \\ \mathbf{C} = \mathbf{C}(\boldsymbol{\theta}) & \text{(3b)} \end{cases}$$

where $\mathbf{C}$ is the stiffness tensor that depends on k constitutive parameters $\boldsymbol{\theta} = (\theta_1, \cdots, \theta_k)$. For instance, an isotropic material depends on $\boldsymbol{\theta} = (K, G)$ where K is the bulk modulus and G the shear modulus.

Set of admissible fields

$$\mathcal{S}(\overline{\boldsymbol{T}}) = \left\{\boldsymbol{\tau} \mid \nabla \cdot \boldsymbol{\tau} = \mathbf{0} \text{ in } \Omega \text{ and } \boldsymbol{\tau} \cdot \boldsymbol{n} = \overline{\boldsymbol{T}} \text{ on } S_f\right\} \tag{4}$$

$$\mathcal{C}(\overline{\boldsymbol{u}}) = \left\{\boldsymbol{v} \mid \boldsymbol{v} = \overline{\boldsymbol{u}} \text{ on } S_u\right\}. \tag{5}$$

where $\mathcal{S}$ and $\mathcal{C}$ are respectively the sets of *statically admissible stress field* and of *kinematically admissible displacement field*. It is worth noting here that the $\boldsymbol{\tau}$ and $\boldsymbol{v}$ fields are independent of each other and not related through any constitutive model.

2.1.2 Principle of Virtual Works (PVW)

The Principle of Virtual Works (PVW) can be expressed from Eq. (1) as [Pierron and Grédiac, 2012]

$$-\int_{\Omega} \boldsymbol{\sigma} : \boldsymbol{\varepsilon}^{\star} \, \mathrm{d}V + \int_{S} \overline{\boldsymbol{T}} \cdot \boldsymbol{u}^{\star} \, \mathrm{d}S = 0 \qquad \forall \, \boldsymbol{u}^{\star} \in \mathcal{C}(\mathbf{0}) \tag{6}$$

where $\boldsymbol{u}^{\star}$ (assumed continuous) and $\boldsymbol{\varepsilon}^{\star} = \frac{1}{2}\left(\nabla \cdot \boldsymbol{u}^{\star} + \nabla^{t} \cdot \boldsymbol{u}^{\star}\right)$ are respectively the virtual displacement and strain fields. $\boldsymbol{u}^{\star} \in \mathcal{C}(\mathbf{0})$ means the virtual field is kinematically admissible such as $\boldsymbol{u}^{\star} = \mathbf{0}$ over S_u in order to vanish the contribution of the unknown prescribed loading over S_u. Both $\boldsymbol{u}^{\star}$ and $\boldsymbol{\varepsilon}^{\star}$ are independent of $\boldsymbol{\sigma}$. Eq. (6) can be divided into the following "physical" quantities:

$$\begin{cases} W_{int}^{\star} = -\displaystyle\int_{\Omega} \boldsymbol{\sigma} : \boldsymbol{\varepsilon}^{\star} \, \mathrm{d}V & \text{Virtual work done by the internal forces} \\ W_{ext}^{\star} = \displaystyle\int_{S} \overline{\boldsymbol{T}} \cdot \boldsymbol{u}^{\star} \, \mathrm{d}S & \text{Virtual work done by the external forces.} \end{cases}$$

Thus, the PVW applied to a body in mechanical equilibrium yields

$$W_{int}^{\star} + W_{ext}^{\star} = 0 \qquad \forall \, \boldsymbol{u}^{\star} \in \mathcal{C}(\mathbf{0}). \tag{7}$$

It should be noted that the virtual quantity $\boldsymbol{u}^{\star}$, also known as virtual displacement, was implicitly assumed to have a length dimension. This provides the convenient "physical" interpretation of the principle of the virtual works for readers with engineering backgrounds. However, this virtual displacement has nothing to do with the actual displacement as it is a purely mathematical function bearing no relation whatsoever to physical quantities. Thus, the physical dimension of the different terms of the PVW depend on the physical dimensions of the virtual quantity.

2.1.3 VFM and constitutive theory identification

The VFM is based on the PVW in which the strain field, denoted by $\widehat{\boldsymbol{\varepsilon}}$, is experimentally determined using full-field measurement techniques. The nature of the material and its constitutive equation are assumed to be known. For example, for an elastic material where $\boldsymbol{\sigma} = \mathbf{C}(\theta_1, \cdots, \theta_k) : \widehat{\boldsymbol{\varepsilon}}$, the governing equation becomes

$$\int_{\Omega} \left[\mathbf{C}(\theta_1, \cdots, \theta_k) : \widehat{\boldsymbol{\varepsilon}} \right] : \boldsymbol{\varepsilon}^{\star} \, \mathrm{d}V = \int_{S_f} \overline{\boldsymbol{T}} \cdot \boldsymbol{u}^{\star} \, \mathrm{d}S \qquad \forall \, \boldsymbol{u}^{\star} \in \mathcal{C}(\mathbf{0}). \tag{8}$$

Then, at least k independent virtual fields must be chosen, among an infinite number of possibilities, to devise a system of k equations whose solution yields the k unknown constitutive parameters. The choice of these virtual fields is a key step. Three main approaches have been studied so far [Avril et al., 2008]:

1. manually using a polynomial function (see the example below);
2. automatically with *special fields* [Grédiac et al., 2002a] that directly supply the constitutive parameters from the virtual work of the external loads. These *special fields* also reduce the technique's noise sensitivity [Avril et al., 2004];
3. piece-wise within the material [Toussaint et al., 2006]. Continuous lower-degree polynomial functions between each sub-region can be used. These latter avoid to use a high-degree polynomial defined on the whole geometry, and which would magnify the noise negative effects.

It should be noted that the volume integral in Eq. (8) requires the knowledge of the strain field in the solid. This is a drawback of the VFM since most of full-field measurement techniques, *e.g.* Digital Image Correlation (DIC), provide in-plane strains over the specimen external surface. Plane stress, plane strain or bending in thin plates loads are typically used to circumvent this limitation.

The VFM was applied to identify the material properties such as

- the in-plane linearly elastic properties of orthotropic composite plates from heterogeneous strain fields [Grédiac et al., 1999, Grédiac et al., 2002b, Toussaint et al., 2006];

- the properties of a non-linearly elastic material assuming a polynomial stress/strain relationship [Grédiac et al., 2002b];
- the bending rigidities of anisotropic thin plates within the framework of the Kirchhoff-Love theory [Grédiac, 1989, Grédiac et al., 2003];
- the stiffness and damping properties of thin viscoelastic isotropic vibrating plates [Giraudeau and Pierron, 2005];
- the properties of a material within a plastic behavior using an iterative procedure based on a minimization process as there is no direct relation between $\boldsymbol{\sigma}$ and the measured strains $\widehat{\boldsymbol{\varepsilon}}$ [Toussaint et al., 2006];
- the damage parameters [Pierron and Grédiac, 2012] within the continuum damage mechanics [Ladeveze and LeDantec, 1992].

All of these examples show that the VFM can be adapted to several kinds of problems. However, in all of them, the success of the VFM relies on the optimal choice of virtual fields.

2.2 Peridynamic (PD) framework

2.2.1 Fundamental equations

In peridynamics [Silling, 2000, Silling and Lehoucq, 2010, Bobaru et al., 2016], a material point located at $\boldsymbol{x}$ interacts with all other material points within a region $\mathcal{H}_{\boldsymbol{x}}$, centered on $\boldsymbol{x}$ and of a radius δ, which is referred to as the horizon (see Fig. 1). These material points in interaction with $\boldsymbol{x}$ are defined in the reference configuration Ω_0 and are not updated over time.

Let a material point be located at $\boldsymbol{x'}$ in $\mathcal{H}_{\boldsymbol{x}}$. Let $\boldsymbol{f_v} = \boldsymbol{f_v}(\boldsymbol{x'}, \boldsymbol{x})$ be the dual force density that a point at $\boldsymbol{x'}$ exerts on a point at $\boldsymbol{x}$. $\boldsymbol{f_v}$ is a force per unit volume squared and has the following properties

$$\begin{cases} \forall\, \boldsymbol{x'} \notin \mathcal{H}_{\boldsymbol{x}} \Longrightarrow \boldsymbol{f_v} = \boldsymbol{0} & \text{(9a)} \\ \boldsymbol{f_v}(\boldsymbol{x}, \boldsymbol{x'}) = -\boldsymbol{f_v}(\boldsymbol{x'}, \boldsymbol{x}) & \text{(9b)} \end{cases}$$

Eq. (9b)'s anti-symmetry results from the reciprocity principle. Thus, $\boldsymbol{f_v}$ can be expressed using the bond force density $\boldsymbol{t_v}$ as

$$\boldsymbol{f_v}(\boldsymbol{x'}, \boldsymbol{x}) = \boldsymbol{t_v}(\boldsymbol{x'}, \boldsymbol{x}) - \boldsymbol{t_v}(\boldsymbol{x}, \boldsymbol{x'}). \tag{10}$$

When assuming that long-range forces (*e.g.*, gravity) are negligible, and similarly to Eqs. (1) and (2), the PD

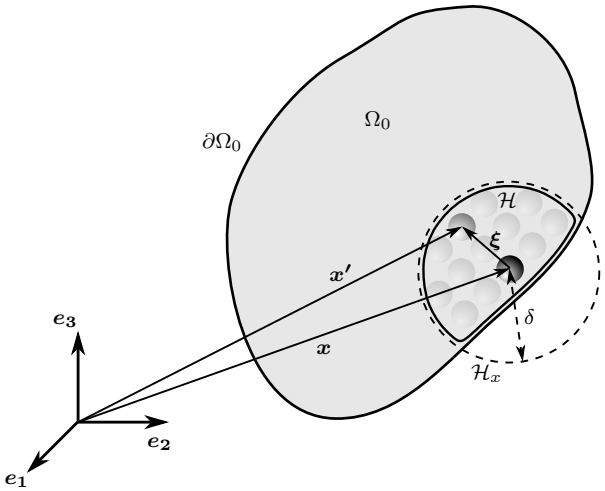

Figure 1: A material point located at $\boldsymbol{x}$ interacts with all other material points within a region $\mathcal{H} = \mathcal{H}_{\boldsymbol{x}} \cap \Omega_0$, centered on $\boldsymbol{x}$ and of a radius δ, which is referred to as the horizon [Delorme, 2018e]

equilibrium equation is

$$\begin{cases} \displaystyle\int_{\mathcal{H}_{\boldsymbol{x}} \cap \Omega_0} \boldsymbol{f_v}(\boldsymbol{x'}, \boldsymbol{x}) \, \mathrm{d}V_{\boldsymbol{x'}} + \boldsymbol{b}(\boldsymbol{x}) = \boldsymbol{0} \qquad \forall \, \boldsymbol{x} \in \Omega & \text{(11a)} \\ \boldsymbol{b} = \overline{\boldsymbol{F}} \text{ on } V_f & \text{(11b)} \\ \boldsymbol{u} = \overline{\boldsymbol{u}} \text{ on } V_u & \text{(11c)} \end{cases}$$

$\overline{\boldsymbol{F}}$ and $\overline{\boldsymbol{u}}$ are the prescribed non-local boundary conditions acting on the boundary volume regions V_f and V_u. These are thin real material layers on the boundary of Ω and are such that $V_f \cup V_u = \partial\Omega$ and $V_f \cap V_u = \emptyset$. $\boldsymbol{b}$ is the external load applied as a body force density, *i.e.*, $\boldsymbol{b} = \boldsymbol{0}$ in $\Omega \setminus V_f$. This is different from classical continuum mechanics in which the boundary conditions are prescribed over the surface $\partial\Omega$.

Fig. 1 shows that the locality of PD depends on the horizon radius δ. In elasticity, it is demonstrated that PD converges to classical continuum mechanics when the horizon approaches zero [Silling and Lehoucq, 2008, Silling and Lehoucq, 2010].

2.2.2 State-based theory

A mathematical object called *states* was developed [Silling et al., 2007, Silling and Lehoucq, 2010] for the state-based theory. The states and their properties are presented in details in App. A of [Delorme et al., 2017]. The main definitions are recalled here.

A vector state is a general mathematical object that maps vectors onto vectors. The well-known second-order tensor can be viewed as a special vector state. In classical continuum mechanics, the constitutive model is expressed through a relationship between the Cauchy stress tensor $\boldsymbol{\sigma}$ and the strain tensor $\boldsymbol{\varepsilon}$. Similarly, a PD constitutive model is expressed with a force state $\underline{\mathbf{T}}$ linked to a deformation state $\underline{\mathbf{Y}}$.

Let $\boldsymbol{x} \in \Omega_0$ and $\boldsymbol{x'} \in \mathcal{H}_{\boldsymbol{x}}$ denote two material points in the reference configuration. Let $\boldsymbol{\xi}$ be the vector defined by $\boldsymbol{\xi} = \boldsymbol{x'} - \boldsymbol{x}$ and called the *bond* connected to $\boldsymbol{x}$. The family $\mathcal{H}$ of $\boldsymbol{x}$ is defined by

$$\mathcal{H} = \left\{ \boldsymbol{\xi} \in \left(\mathbb{R}^3 \setminus \boldsymbol{0} \right) \mid (\boldsymbol{\xi} + \boldsymbol{x} = \boldsymbol{x'}) \in (\mathcal{H}_{\boldsymbol{x}} \cap \Omega_0) \right\} \tag{12}$$

where $\mathcal{H}$ and $\mathcal{H}_{\boldsymbol{x}}$ are schematized in Fig. 1.

Let $\underline{\mathbf{Y}}$ be the deformation state that transforms bonds $\boldsymbol{\xi}$ connected to $\boldsymbol{x}$ to their deformed images as

$$\forall \boldsymbol{\xi} \in \mathcal{H}, \quad \underline{\mathbf{Y}}[\boldsymbol{x}] \langle \boldsymbol{\xi} \rangle = \boldsymbol{y}(\boldsymbol{x} + \boldsymbol{\xi}) - \boldsymbol{y}(\boldsymbol{x}) = \boldsymbol{y}(\boldsymbol{x'}) - \boldsymbol{y}(\boldsymbol{x}) \in \mathbb{R}^3 \tag{13}$$

where $\boldsymbol{y}(\boldsymbol{x})$ and $\boldsymbol{y}(\boldsymbol{x'})$ are, respectively, the deformed positions of $\boldsymbol{x}$ and $\boldsymbol{x'}$. Fig. 2 illustrates these variables. It is further assumed that

$$\forall (\boldsymbol{x_1}, \boldsymbol{x_2}) \in \Omega_0^2 \mid \boldsymbol{x_1} \neq \boldsymbol{x_2} \Longrightarrow \boldsymbol{y}(\boldsymbol{x_1}) \neq \boldsymbol{y}(\boldsymbol{x_2}) \Longrightarrow \underline{\mathbf{Y}}[\boldsymbol{x}] \langle \boldsymbol{\xi} \rangle \neq \boldsymbol{0}, \tag{14}$$

which means that two distinct points in the reference configuration Ω_0 are also distinct in the deformed configuration Ω_t. Thus, the deformed direction vector state $\underline{\mathbf{M}}$ is defined by

$$\underline{\mathbf{M}} = \frac{\underline{\mathbf{Y}}}{|\underline{\mathbf{Y}}|}. \tag{15}$$

The force state $\underline{\mathbf{T}}$ is related to the bond force density $\boldsymbol{t_v}$ through

$$\forall \boldsymbol{\xi} \in \mathcal{H}, \quad \underline{\mathbf{T}}[\boldsymbol{x}] \langle \boldsymbol{\xi} \rangle = \underline{\mathbf{T}}[\boldsymbol{x}] \langle \boldsymbol{x'} - \boldsymbol{x} \rangle = \boldsymbol{t_v}(\boldsymbol{x'}, \boldsymbol{x}) \in \mathbb{R}^3. \tag{16}$$

Combining Eqs. (9), (11a) and (16) leads to the PD equilibrium equation such as, $\forall \, \boldsymbol{x} \in \Omega_0$,

$$\begin{cases} \displaystyle\int_{\Omega_0} \Big(\underline{\mathbf{T}}[\boldsymbol{x}] \langle \boldsymbol{x'} - \boldsymbol{x} \rangle - \underline{\mathbf{T}}[\boldsymbol{x'}] \langle \boldsymbol{x} - \boldsymbol{x'} \rangle \Big) \, \mathrm{d}V_{\boldsymbol{x'}} + \boldsymbol{b}(\boldsymbol{x}) = \boldsymbol{0} & \text{(17a)} \\ \boldsymbol{f_v}(\boldsymbol{x'}, \boldsymbol{x}) = \underline{\mathbf{T}}[\boldsymbol{x}] \langle \boldsymbol{x'} - \boldsymbol{x} \rangle - \underline{\mathbf{T}}[\boldsymbol{x'}] \langle \boldsymbol{x} - \boldsymbol{x'} \rangle & \text{(17b)} \end{cases}$$

App. B of [Delorme et al., 2017] presents the three PD constitutive models which are the *bond-based*, the *ordinary state-based* and *non ordinary state-based* theories. In the sequel, only the ordinary state based approach is used since isotropic linearly elastic materials are considered.

2.2.3 2D ordinary state-based model for linearly isotropic elasticity

This section provides the constitutive models for an linearly isotropic elastic material under plane stress and plane strain (see App. A for details).

2D plane stress constitutive model

$$\begin{cases} \underline{\mathbf{T}} = \left\{ \frac{1}{3} \left[2 \left(\frac{2\nu - 1}{\nu - 1} \right) \alpha^s + \left(\frac{\nu + 1}{\nu - 1} \right) \alpha^d \right] \underline{w}\, \underline{e}^s + \alpha^d\, \underline{w}\, \underline{e}^d \right\} \underline{\mathbf{M}} & \text{(18a)} \\ \alpha^s = \frac{1}{q} \left[9K + G \left(\frac{\nu + 1}{2\nu - 1} \right)^2 \right] & \text{(18b)} \\ \alpha^d = \frac{1}{q} (8G) & \text{(18c)} \end{cases}$$

where α^s and α^d are the spherical and deviatoric PD parameters, $\underline{e}^s$ and $\underline{e}^d$ the spherical and deviatoric extension state, ν the Poisson's ratio and q the PD weighted volume (see Eq. (37) and [Silling et al., 2007] for more details).

2D plane strain constitutive model

$$\begin{cases} \underline{\mathbf{T}} = \left\{ \frac{1}{3} \left(2\alpha^s - \alpha^d \right) \underline{w}\, \underline{e}^s + \alpha^d\, \underline{w}\, \underline{e}^d \right\} \underline{\mathbf{M}} & \text{(19a)} \\ \alpha^s = \frac{1}{q} (9K + G) & \text{(19b)} \\ \alpha^d = \frac{1}{q} (8G) & \text{(19c)} \end{cases}$$

2.2.4 Discretization

Several approaches have been used to discretize the PD equilibrium equation (17) such as Galerkin finite element methods [Chen and Gunzburger, 2011], Gauss quadrature [Weckner and Emmrich, 2005], the spatial discretization [Emmrich and Weckner, 2007, Parks et al., 2008] or the EMU (name of the first PD software implemented [Littlewood, 2015]) nodal discretization (ND). The last method (EMU-ND) consists of a mid-point (or one-point) quadrature in a Lagrangian spatial discretization. The EMU-ND has been chosen for its efficient load distribution scheme and acceptable computation time. Fig. 3 shows the mesh of a reference position in 2D with regularly spaced nodes where h is the fixed mesh size. Each node i, located at $\boldsymbol{x}_i$ in the

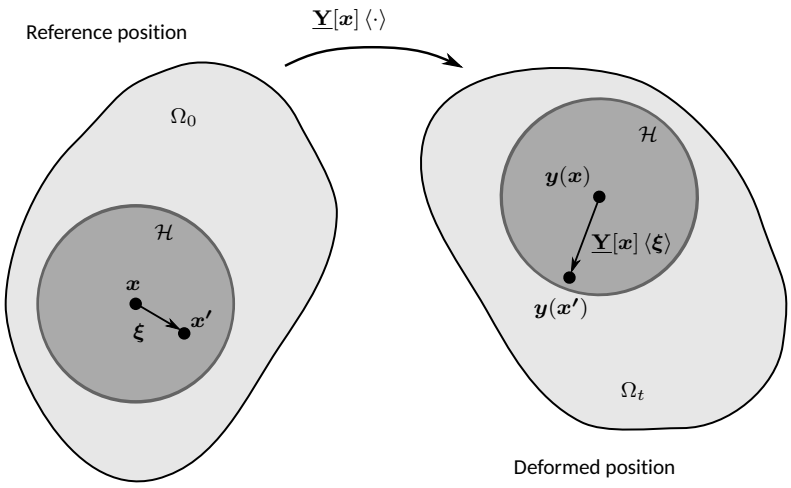

Figure 2: The deformation state $\underline{\mathbf{Y}}$ transforms bonds $\boldsymbol{\xi} \in \mathcal{H}$ to their deformed images. $\boldsymbol{y}(\boldsymbol{x})$ and $\boldsymbol{y}(\boldsymbol{x'})$ are, respectively, the deformed positions of $\boldsymbol{x}$ and $\boldsymbol{x'}$ [Delorme, 2018c].

dual mesh, is associated to a fixed volume V_i. Assume that the volumes surrounding the nodes are non overlapping ($V_i \cap V_j = \emptyset$), and are recovering the reference volume V_Ω, meaning that $\sum_i^n V_i = V_\Omega$. The discrete family $\mathcal{H}_i$ of a node i is defined by:

$$\mathcal{H}_i = \{j \mid \boldsymbol{x}_j \in \Omega_0 \text{ and } \|\boldsymbol{\xi_i}\|_2 = \|\boldsymbol{x}_j - \boldsymbol{x}_i\|_2 \leq \delta\} \tag{20}$$

Thus, the discrete PD equilibrium equation under the EMU-ND scheme, and which has to numerically be solved for each node i, reads

$$\begin{cases} \displaystyle\sum_{j \in \mathcal{H}_i} \Big(\underline{\mathbf{T}}[\boldsymbol{x}_i] \langle \boldsymbol{x}_j - \boldsymbol{x}_i \rangle - \underline{\mathbf{T}}[\boldsymbol{x}_j] \langle \boldsymbol{x}_i - \boldsymbol{x}_j \rangle \Big) V_j + \boldsymbol{b}_i = \mathbf{0} & \text{(21a)} \\ \boldsymbol{f_v}(\boldsymbol{x}_j, \boldsymbol{x}_i) = \underline{\mathbf{T}}[\boldsymbol{x}_i] \langle \boldsymbol{x}_j - \boldsymbol{x}_i \rangle - \underline{\mathbf{T}}[\boldsymbol{x}_j] \langle \boldsymbol{x}_i - \boldsymbol{x}_j \rangle & \text{(21b)} \end{cases}$$

where $\boldsymbol{b}_i$ is the external load applied to the node i. Recall that $\boldsymbol{b}_i = \mathbf{0}$ if node i is not on an external layer of the body where the external load is applied.

One drawback reducing the accuracy of this discretization is the treatment of nodes j whose V_j is partially inside the horizon of a node i and partially outside (see Fig. 3). Several algorithms were evaluated [Seleson, 2014] to improve the accuracy of the discretization using partial areas taking into account the fraction that is outside the horizon. The most common is the PA-PDLAMMPS algorithm [Parks et al., 2008] which has been implemented in the code [Delorme et al., 2018] presented in Sec. 5.

3 The Virtual Fields Method within Peridynamics

3.1 Principle of Virtual Works

Since Eq. (17) is valid for any $x \in \Omega_0$, each term can be "multiplied" (using the Euclidean inner product) by any continuous vector function $\boldsymbol{u}^\star$ such as

$$\left(\int_{\Omega_0} \boldsymbol{f_v}(\boldsymbol{x'}, \boldsymbol{x}) \, \mathrm{d}V_{\boldsymbol{x'}} + \boldsymbol{b}(\boldsymbol{x}) \right) \cdot \boldsymbol{u}^\star(\boldsymbol{x}) = 0. \tag{22}$$

Integrating Eq. (22) over the whole domain Ω_0 yields the PVW stated as

$$\int_{\Omega_0} \int_{\Omega_0} \boldsymbol{f_v}(\boldsymbol{x'}, \boldsymbol{x}) \cdot \boldsymbol{u}^\star(\boldsymbol{x}) \, \mathrm{d}V_{\boldsymbol{x'}} \, \mathrm{d}V_{\boldsymbol{x}} + \int_{\Omega_0} \boldsymbol{b}(\boldsymbol{x}) \cdot \boldsymbol{u}^\star(\boldsymbol{x}) \, \mathrm{d}V_{\boldsymbol{x}} = 0. \tag{23}$$

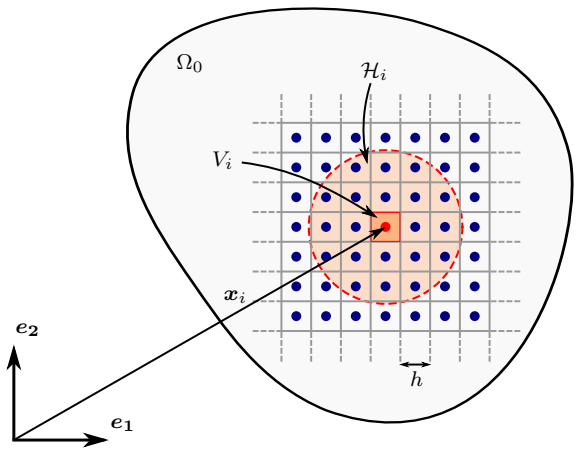

Figure 3: 2D EMU-ND and its mesh with a constant mesh size h. V_i is the surrounding volume of the node i located at $\boldsymbol{x}_i$ and $\mathcal{H}_i$ its discrete family. The integration over $\mathcal{H}_x$ from Eq. (11) is now replaced by the discrete sum fron Eq. (21) over $\mathcal{H}_i$ [Delorme, 2018d].

Assume that the virtual quantity $\boldsymbol{u}^\star$ is kinematically admissible, *i.e.* $\boldsymbol{u}^\star \in \mathcal{C}(\mathbf{0})$, then, the contribution of the unknown force over the boundary volume constraint region V_u vanishes. Eq. (23) can be divided into the following "physical" quantities:

$$\begin{cases} \mathcal{W}_{int}^\star = \displaystyle\int_{\Omega_0}\int_{\Omega_0} \boldsymbol{f_v}(\boldsymbol{x'}, \boldsymbol{x}) \cdot \boldsymbol{u}^\star(\boldsymbol{x}) \, \mathrm{d}V_{\boldsymbol{x'}} \, \mathrm{d}V_{\boldsymbol{x}} & \text{(24a)} \\ \mathcal{W}_{ext}^\star = \displaystyle\int_{\Omega_0} \boldsymbol{b}(\boldsymbol{x}) \cdot \boldsymbol{u}^\star(\boldsymbol{x}) \, \mathrm{d}V_{\boldsymbol{x}} & \text{(24b)} \end{cases}$$

where $\mathcal{W}_{int}^\star$ is the virtual work done by the internal dual force densities and $\mathcal{W}_{ext}^\star$ the virtual work done by the external forces. As for CCM version of the PVW, $\mathcal{W}_{int}^\star + \mathcal{W}_{ext}^\star = 0$.

3.2 Virtual Fields Method and material identification

The PD ordinary state-based constitutive equations for linearly isotropic elasticity depend non-linearly on the material properties (Eqs. (18) and (19)). Because of this non-linear relationship, the k sought material parameters are solution of a non-linear system. Rather than explicitly solving this non-linear system, the non-linear set of at least k independent equations were solved by minimizing a residual function Φ. Since linearly isotropic elastic materials are considered, Φ requires at least two independent virtual fields $\boldsymbol{u}^{\star(k)}$ to properly identify the material parameters (K, G). Thus, the residual function Φ, defined as a normalized squared residual between $\mathcal{W}_{int}^\star$ and $\mathcal{W}_{ext}^\star$, was

$$\Phi(K; G) = \sqrt{\frac{\displaystyle\sum_{k=1}^{M\geq 2} \left(\mathcal{W}_{int}^{\star(k)} + \mathcal{W}_{ext}^{\star(k)}\right)^2}{\displaystyle\sum_{k=1}^{M\geq 2} \left(\mathcal{W}_{ext}^{\star(k)}\right)^2}}, \tag{25}$$

Note that the normalization was used only for comparison purpose. Also, it was assumed that $\boldsymbol{u}^{\star(k)}$ are such that $\displaystyle\sum_k \left(\mathcal{W}_{ext}^{\star(k)}\right)^2 \neq 0$.

4 Case study: three-point bending test

4.1 Geometry and boundary conditions

Fig. 4 describes a virtual three-point bending setup in which a beam, of dimensions $L \times W \times t$ (length $\times$ width $\times$ thickness) and simply supported on two supports spaced of S. The coordinate system $(O, \boldsymbol{e_1}, \boldsymbol{e_2})$ origin lies in the specimen's middle, on its bottom line. The beam is submitted to an external force applied to the specimen's top surface center as

$$\boldsymbol{F}(0, W) = -F \cdot \boldsymbol{e_2} \tag{26}$$

4.2 The virtual displacement fields definition

Two trivial independent continuous virtual displacement fields $\boldsymbol{u}^{\star(1)}$ and $\boldsymbol{u}^{\star(2)}$ were defined:

$$\boldsymbol{u}^{\star(1)}(x_1, x_2) = \left(|x_1| - \frac{S}{2}\right) \cdot \boldsymbol{e_2} \tag{27}$$

$$\boldsymbol{u}^{\star(2)}(x_1, x_2) = \left(|x_1| \, \frac{x_1 \, x_2}{L \, W}\right) \cdot \boldsymbol{e_1} \tag{28}$$

These virtual fields, depicted in Fig. 5, are kinematically admissible, *i.e.* they vanish on the supports:

$$\boldsymbol{u}^{\star(1)}\left(\pm\frac{S}{2}, 0\right) = \boldsymbol{u}^{\star(2)}\left(\pm\frac{S}{2}, 0\right) = \mathbf{0}. \tag{29}$$

4.3 Application of the Virtual Field Method

The internal virtual works $\mathcal{W}_{int}^{\star}$ were approximated from Eqs. (21) and (24a) as

$$\mathcal{W}_{int}^{\star} = \sum_{i} \sum_{j \in \mathcal{H}_i} \Big(\boldsymbol{f_v}(\boldsymbol{x}_j, \boldsymbol{x}_i) \cdot \boldsymbol{u}_i^{\star} \Big) V_j \, V_i. \tag{30}$$

The external virtual works $\mathcal{W}_{ext}^{\star}$ were calculated from Eq. (24b) and are equal to:

$$\begin{cases} \mathcal{W}_{ext}^{\star(1)} = \boldsymbol{F} \cdot \boldsymbol{u}_A^{\star(1)} = \boldsymbol{F} \cdot \boldsymbol{u}^{\star(1)}(0, W) = \dfrac{FS}{2} & \text{(31a)} \\ \\ \mathcal{W}_{ext}^{\star(2)} = \boldsymbol{F} \cdot \boldsymbol{u}_A^{\star(2)} = \boldsymbol{F} \cdot \boldsymbol{u}^{\star(2)}(0, W) = 0 & \text{(31b)} \end{cases}$$

Finally, K and G were extracted using the residual function Φ from Eq. (25) and the minimization process described in Sec. 5.

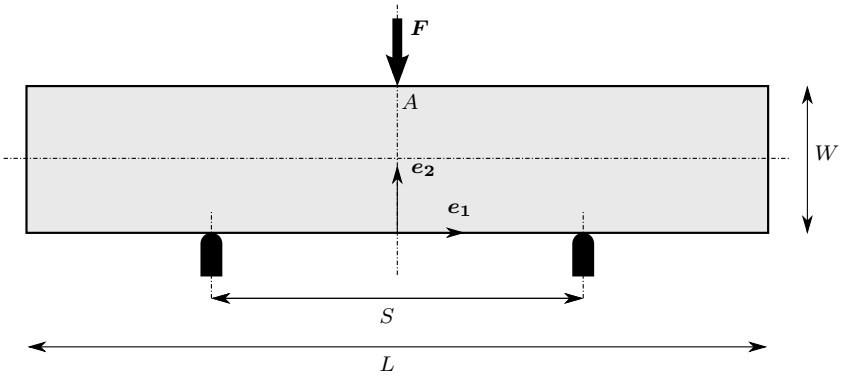

Figure 4: Three-point bending setup in which a beam, of dimensions $L \times W \times t$ and simply supported on two supports spaced of S, is submitted to an external force $\boldsymbol{F}$. The coordinate system $(O, \boldsymbol{e_1}, \boldsymbol{e_2})$ origin is located at the specimen's bottom face center [Delorme, 2018a].

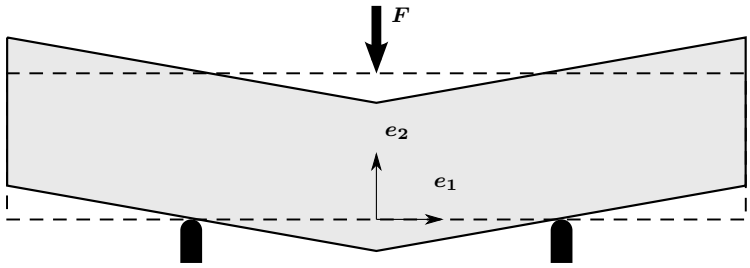

(a) Shape of the first virtual field $\boldsymbol{u}^{\star(1)}$

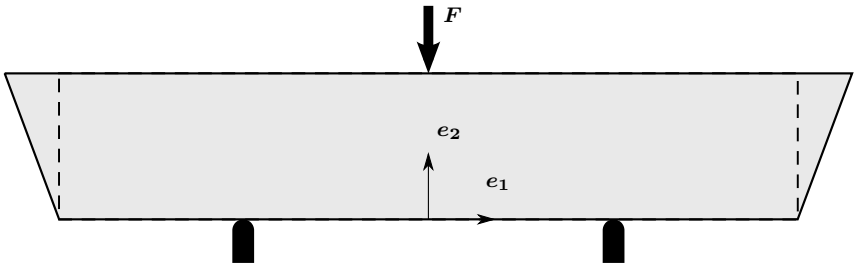

(b) Shape of the second virtual field $\boldsymbol{u}^{\star(2)}$

Figure 5: Virtual displacements applied to the three-point bending test. The coordinate system $(O, \boldsymbol{e_1}, \boldsymbol{e_2})$ origin is located at the specimen's bottom face center [Delorme, 2018f].

5 Minimization process implementation

5.1 Algorithm

Fig. 6 shows the algorithm state chart diagram used for the minimization process to extract the material properties from the actual displacement field. The algorithm has in input the initial guess for the material properties $(K; G)$ and the actual displacement field $\widehat{\boldsymbol{u}}$. A uniformly distributed random value in a search interval I sufficiently large to the include material's expected properties was chosen as the initial guess. The gathered steps in the box (see Fig. 6) are repeated until the residual Φ is smaller or equal to a fixed tolerance ϵ. The main steps are described below:

1. The dual force density $\boldsymbol{f_v}$ is computed from Eq. (21) using the trial material properties and $\widehat{\boldsymbol{u}}$. For this step, the in-house state-based PD code *PeriPyDIC* [Delorme et al., 2018] is used with the 2D constitutive modeling described in Sec. 2.2.3). Note that instead of solving a direct problem in which the displacement field is computed from the boundary conditions, here the dual force density $\boldsymbol{f_v}$ is evaluated from a provided displacement field.

2. The internal virtual works $\mathcal{W}^{\star}_{int}$ are computed from Eq. (30) with the in-house code *PeriPyVFM* [Delorme and Diehl, 2018], with the two virtual fields given in Eqs. (27) and (28). Note that *PeriPyVFM* is based on the discretized version of the equations given in Sec. 3 and can be extended to as many virtual fields as required.

3. The residual Φ defined in Eq. (25) is computed within *PeriPyVFM* using $\mathcal{W}^{\star}_{int}$ and the external virtual works $\mathcal{W}^{\star}_{ext}$ calculated from Eq. (31).

As long as the residual Φ is greater than the tolerance ϵ, the "black box" optimization solver *NOMAD* [Le Digabel, 2011], which implements the mesh adaptive direct search (MADS) algorithm, provides the new guess for the material properties. Thus, the three steps inside the box are repeated until black box minimization finds suitable values for the material properties and the algorithm terminates. Table 1 summarizes the versions of the software used in this paper.

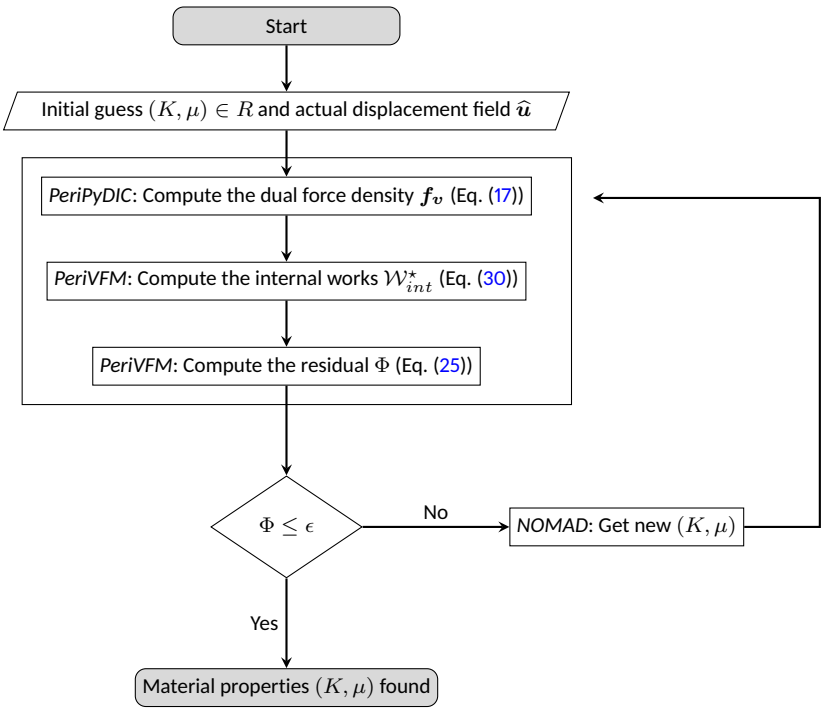

Figure 6: State chart diagram of the algorithm to extract the material properties from the actual displacement field. The non-linear black box optimization software *NOMAD* [Le Digabel, 2011], based on the MADS algorithm, is used for the minimization process.

5.2 Choice of the horizon δ

Choosing the ratio δ/h of horizon and nodal spacing to gain convergence is still an open question within the PD community [Bobaru et al., 2009, Bobaru and Hu, 2012]. Local limits and asymptotically compatible discretizations were considered in [Du and Tian, 2015] and [Du, 2016]. It is shown in [Tian and Du, 2013] that, if the nodal spacing $h \to 0$ decays faster than the horizon $\delta \to 0$, the EMU-ND converges to the continuum local partial differential equation (PDE) limit. An empirical choice of the horizon for a specific material is to adjust the horizon to fit experimental results. Convergence analysis can also be performed as described in [Bobaru et al., 2009] in which three types of convergence are presented: the δ-, m- and (δm)-convergence where $m = \delta/h$.

The approach used in this paper assumes the use of experimental data. In that case, the nodal spacing h is more or less prescribed by the measuring equipment resolution, *e.g.*, the DIC system. As the horizon is such as $\delta = mh$, m is the only parameter to adjust with respect to the residual function Φ. Thus, a three-point bending test simulated by finite element with a mesh-size of $h = 0.25$ mm was used to calibrate m. The residual Φ was computed for the exact material properties for different value of m. Fig. 7 plots Φ as a function of m. It can be seen that Φ is large for $m \geq 2$, gets smaller for the next values and is the smallest for $m = 7$. Then, Φ increases for the next two values. This kind of non stabilized behavior has been shown in [Diehl et al., 2016]. Therefore, $m = 7$ was used in the sequel to extract the material properties (K, G) using the algorithm presented in Fig. 6. Note that this is not a convergence study but only a simplistic way to choose the horizon δ.

Table 1: Software used for the implementation of the state-based PD-VFM.

Name	Version	Reference
NOMAD	3.8	[Le Digabel, 2011]
PeriPyDIC	0.1	[Delorme et al., 2018]
PeriPyVFM	0.1	[Delorme and Diehl, 2018]

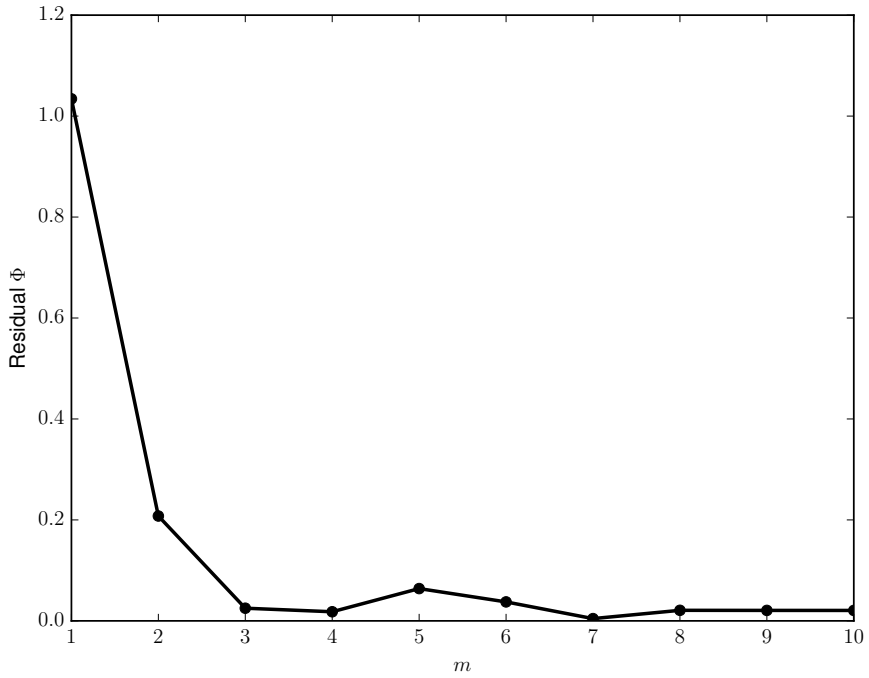

Figure 7: Residual Φ for the different m-values with $h = 0.25$ mm. The objective of this simplistic analysis is to find the best m-value to use in the PD model in order to obtain the smallest residual Φ for the prescribed mesh-size.

6 Numerical validation

6.1 Actual displacements simulated by Finite Element Analysis

The virtual three-point bending test presented in Fig. 4 was modelled in finite element analysis (FEA) with ANSYS®. The setup size parameters were: $L = 128\,\text{mm}$, $W = 32\,\text{mm}$, $t = 12.7\,\text{mm}$ and $S = 96\,\text{mm}$. The geometry was discretized using the PLANE182 2-D Structural Solid element with a mapped meshing of $h = 0.25\,\text{mm}$. The element was used as a plane stress element and was defined by four nodes having two translations at each node in $\boldsymbol{e_1}$ and $\boldsymbol{e_2}$ directions. A null displacement condition was applied to the nodes located on the two supports and the beam was loaded with a force of magnitude F of $1\,000\,\text{N}$ applied to node A shown in Fig. 4. The Young's modulus E was of $4\,000\,\text{MPa}$ and the Poisson's ratio ν of 0.3, which yields a bulk modulus $K = 3\,333.33\,\text{MPa}$ and a shear modulus $G = 1\,538.46\,\text{MPa}$. Figs. 8a and 8b respectively show the components u_1 and u_2 for the simulated displacement field $\widehat{\boldsymbol{u}}_{\text{FEA}}$.

6.2 Extracted material properties using the displacement field

The displacement field $\widehat{\boldsymbol{u}}_{\text{FEA}}$ was input in the algorithm described in Sec. 5 to identify the material properties. The search interval for the sought (K, G) was $I = [1\,000; 10\,000]^2$. This interval includes the entered values $K = 3\,333.33\,\text{MPa}$ and $G = 1\,538.46\,\text{MPa}$. Based on Eq. (31), the external virtual works were $\mathcal{W}_{ext}^{\star(1)} = 48\,000\,\text{N mm}$ and $\mathcal{W}_{ext}^{\star(2)} = 0\,\text{N mm}$. The extracted material properties are presented in Table 2.

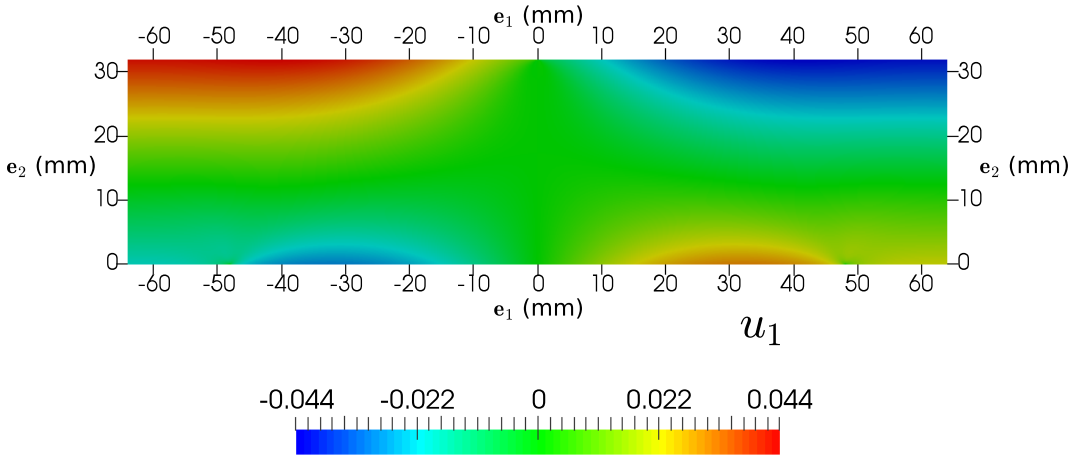

(a) u_1-component of the displacement field $\widehat{\boldsymbol{u}}_{\text{FEA}}$.

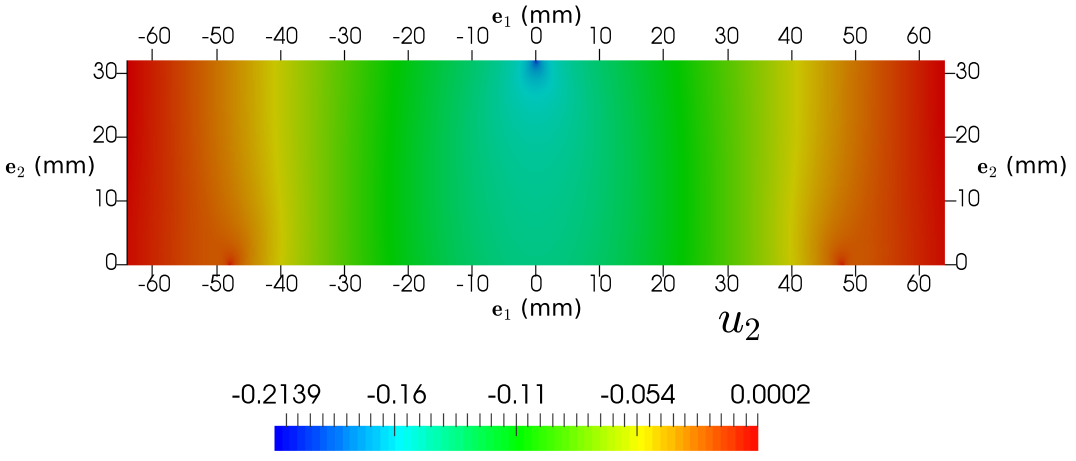

(b) u_2-component of the displacement field $\widehat{\boldsymbol{u}}_{\text{FEA}}$.

Figure 8: Components u_1 (a) and u_2 (b) of the simulated displacement field $\widehat{\boldsymbol{u}}_{\text{FEA}}$.

When the initial guesses for K and G were exactly in the mid of the search interval I, *i.e.* $(K;G) = (5\,000;5\,000)$, the relative errors with respect to the material properties fed in the FEM were $\epsilon_K = 0.63\%$ for the bulk modulus and $\epsilon_G = -0.44\%$ for the shear modulus. The extracted properties using the state-based PD-VFM are in good agreement with those utilized in the FEA.

The minimization was run 14 more times with different initial guesses distributed within the search interval to investigate the method's robustness and stability. Table 2 gathers the results and shows that all the extracted material properties converge to the same values (they only differ for the fourth decimal point), even though the number of evaluations was different. Therefore, the minimization of the residual Φ seems to be stable and means that exactly one global minimum must exist within the search interval.

6.3 Noise analysis

The actual displacement field $\widehat{\boldsymbol{u}}_{\text{FEA}}$ used to identify the properties was optimal with respect to bias and noise as this is a simulated field. Thus, the slight differences between the actual material properties fed in the FEM and those extracted could be attributed to several sources such as the error induced with the discretization scheme, the so-called PD surface effect [Le and Bobaru, 2017], the numerical round off errors or the virtual field chosen which can be more or less sensitive to the previous errors effects [Pierron and Grédiac, 2012].

Real displacement fields are disturbed both by bias and noise [Sutton et al., 2009]. Contrary to the DIC bias that can be reduced or eliminated with a proper setup and parameters (good calibration, no contamination or dust, no aliasing), the noise is unavoidable even though it can be minimized with a careful setup (good focus and speckle pattern, contrast, lighting, stereo-angle, lens selection). A noise analysis simulating experimental data was performed by adding a Gaussian noise term to disturb $\widehat{\boldsymbol{u}}_{\text{FEA}}$ as

$$\begin{cases} \widehat{\boldsymbol{u}}_{\text{NOISE}} = \widehat{\boldsymbol{u}}_{\text{FEA}} + \boldsymbol{g}_{\text{NOISE}} & \text{(32a)} \\ \boldsymbol{g}_{\text{NOISE}} = g_1 \cdot \boldsymbol{e_1} + g_2 \cdot \boldsymbol{e_2} & \text{(32b)} \end{cases}$$

where $\boldsymbol{g}_{\text{NOISE}}$ is the disturbing displacement vector whose components g_1 and g_2 follow a Gaussian distribution of mean μ and standard deviation Σ. It was assumed that $\mu = 0.0$ mm, and Σ lied between 0.0 and 2.5×10^{-4} mm which is a typical standard deviation range measured with the DIC-system used in the Laboratory for Multiscale Mechanics (LM2).

Table 2: Extracted material properties from $\widehat{\boldsymbol{u}}_{\text{FEA}}$. 15 initial guesses $(K;G) \in [1\,000;10\,000]^2$ were used and provided in the second and third columns. The fourth and fifth columns represent the extracted material properties after minimization. The sixth and seventh columns show the relative error with respect to the material properties used in the FEA, which are $(K;G) = (3\,333.33;1\,538.46)$. The last column shows the number of evaluations performed with the *NOMAD* solver.

	Initial guesses		Minimization results		Relative error		
#	K (MPa)	G (MPa)	K (MPa)	G (MPa)	ϵ_K (%)	ϵ_G (%)	Eval
1	5 000.000	5 000.000	3 354.194	1 531.635	0.63	−0.44	435
2	1 098.722	7 031.443	3 354.194	1 531.635	0.63	−0.44	508
3	2 495.136	6 502.603	3 354.194	1 531.635	0.63	−0.44	493
4	9 845.479	1 797.806	3 354.194	1 531.635	0.63	−0.44	509
5	1 858.444	9 782.045	3 354.194	1 531.635	0.63	−0.44	532
6	4 334.080	5 263.272	3 354.194	1 531.635	0.63	−0.44	510
7	6 410.611	3 680.783	3 354.194	1 531.635	0.63	−0.44	450
8	9 881.218	2 116.642	3 354.194	1 531.635	0.63	−0.44	390
9	8 723.166	7 719.498	3 354.194	1 531.635	0.63	−0.44	427
10	3 718.518	6 977.810	3 354.194	1 531.635	0.63	−0.44	431
11	8 486.055	9 008.744	3 354.194	1 531.635	0.63	−0.44	541
12	3 396.443	6 769.252	3 354.194	1 531.635	0.63	−0.44	538
13	5 543.759	3 163.586	3 354.194	1 531.635	0.63	−0.44	515
14	5 723.661	6 488.884	3 354.194	1 531.635	0.63	−0.44	435
15	4 612.369	1 874.837	3 354.194	1 531.635	0.63	−0.44	543

Table 3 provides the extracted material properties after adding Gaussian noise. The relative error remained under 1.4% in absolute value. Therefore, the virtual fields chosen seem stable with respect to noise. This could be different with other virtual fields. Also, it should be noted that the bulk modulus K is more sensitive to Gaussian noise than the shear modulus G. The conclusion from this noise analysis is similar that presented in [Kramer and Scherzinger, 2014], in which the VFM is applied within CCM.

6.4 Missing data

Obtaining displacement fields on the exact specimen edges is hardly possible with DIC and the missing data due to this experimental limitation could have a significant influence on the identification results, depending the the virtual fields chosen [Pierron and Grédiac, 2012]. Lines of elements that were placed of a multiple of $h = 0.25\,\text{mm}$ have been removed from the specimen's edges (see Fig. 9) before extracting the material properties to simulate the effect of the missing data.

Fig. 10 presents the effects of these missing nodes on the residual Φ. A linear relation can be highlighted, showing the necessity to obtain data as close as possible to the free edges to accurately extract the material properties. Table 4 provides the error in the identification of K and G, showing that the relative errors quickly increase for the bulk modulus K. This means the identification of K is more sensitive to missing data than the shear modulus G using the three-point bending experimental setup and the virtual fields defined in Eqs. (27) and (28).

7 Conclusion

The main contributions of this study are as follows:

1. The VFM within PD has been derived to extract the elastic properties of a linearly isotropic material. Open-source python codes [Delorme and Diehl, 2018, Delorme et al., 2018] including a minimization process have also developed to implement the PD-VFM. Contrary to most other approaches existing in the PD literature, one of the benefits of the PD-VFM is that no computation of the displacement field during the minimization process is required.
2. The PD-VFM has been tested on a three-point bending test using undisturbed displacement fields

Table 3: Error in the identification of K and G due to Gaussian noise. The first column is the noise's standard deviation Σ used. The second and third columns represent the extracted material properties after minimization. The fourth and fifth columns show the relative error with respect to the material properties use in the FEA, which are $(K; G) = (3\,333.33; 1\,538.46)$

Standard Deviation	Minimization results		Relative error	
Σ (mm)	K (MPa)	G (MPa)	ϵ_K (%)	ϵ_G (%)
0.0×10^{-4}	3 354.194	1 531.635	0.63	−0.44
0.5×10^{-4}	3 347.890	1 531.918	0.44	−0.43
1.0×10^{-4}	3 379.440	1 531.790	1.38	−0.43
1.5×10^{-4}	3 339.325	1 531.485	0.18	−0.45
2.0×10^{-4}	3 323.665	1 532.692	−0.29	−0.37
2.5×10^{-4}	3 364.742	1 533.479	0.94	−0.32

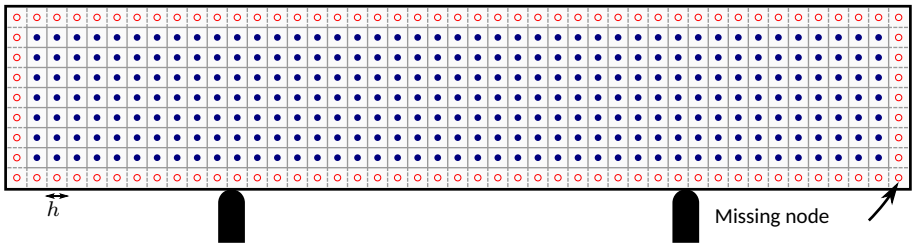

Figure 9: Missing nodes all around the specimen's edges [Delorme, 2018b].

generated by FEA and two independent virtual fields arbitrarily chosen. The material properties extracted with the PD-VFM were in a quasi-perfect agreement with those utilized in the FEA. This numerical validation of the PD-VFM shows the robustness of the approach. Both the stability and the sensibility against noise and missing data have also been studied. The latter highlighted a linear relation between these missing data and the residual Φ, showing the necessity to obtain data as close as possible to the free edge to accurately extract the material properties.

Even though the numerical validation of the PD-VFM led to remarkable results, meaning the material properties identification within less than 0.75% error, there is still a scope for enhancing the solver performance and reduce the calculation time. Also, the authors tried to apply the PD-VFM to experimental DIC measurements performed on a polycarbonate beam under a three-point bending test. However, the residual Φ computed using the actual material properties (measured per ASTM D638-14) was too high and then did not allow to extract the material properties. This can be explained by the difficulty of reducing the missing data due to the DIC measurements and the high sensibility of the bulk modulus K with respect to this missing information and virtual fields chosen. Based on the full-field measurement literature [Belhabib et al., 2008, Pierron and Grédiac, 2012], the authors would recommend to design a well-suited test configuration for the PD-VFM that would meets the following criteria:

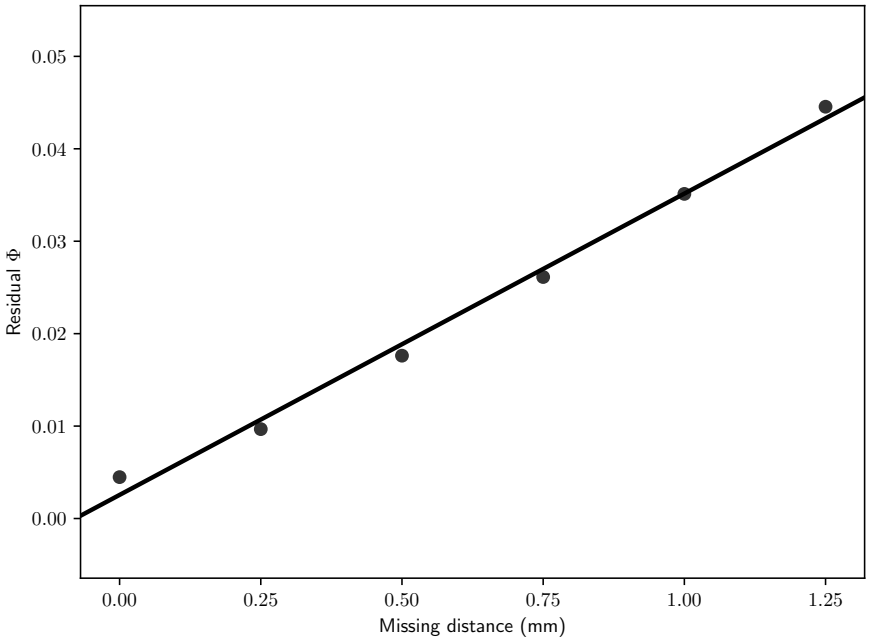

Figure 10: Influence of missing data: the black line shows the linear regression between the residual Φ with respect to the missing distance around the specimen.

Table 4: Error in the identification of K and G due to the missing data on the specimen free edges. The first column is the missing distance on the edge (see Fig. 9). The second and third columns represent the extracted material properties after minimization. The fourth and fifth columns show the relative error with respect to the material properties used in the FEA, which are $(K; G) = (3\,333.33; 1\,538.46)$

Missing distance	Minimization results		Relative error	
mm	K (MPa)	G (MPa)	ϵ_K (%)	ϵ_G (%)
0.00	3 354.194	1 531.635	0.63	−0.44
0.25	3 577.209	1 552.676	7.32	0.92
0.50	3 708.762	1 565.134	11.26	1.73
0.75	3 853.462	1 578.672	15.60	2.61
1.00	4 011.848	1 593.237	20.36	3.56
1.25	4 184.931	1 608.811	25.55	4.57

- a large heterogeneity of the displacement fields. This is the spirit of the full-field measurement methods, by opposition to standard mechanical tests that are based on homogeneous and averaged fields;
- a good sensitivity of the displacement fields with respect to the material properties to identify.

The authors also point out that they were only interested in this study to present a proof of concept of the PD-VFM by extracting the elastic properties of a linearly isotropic material. However, they believe that future works could use the approach presented through this paper and extend it for damage characterization, which is the main strength of PD.

A Isotropic elastic materials within state-based peridynamics

A.1 Elastic material

An elastic material is defined by its free energy density ψ which only depends on $\underline{\mathbf{Y}}$. Define $\psi = \Psi(\underline{\mathbf{Y}})$ as the *strain energy density*. Then, the force state $\underline{\mathbf{T}}$ is defined by

$$\underline{\mathbf{T}} = \underline{\mathbf{T}}(\underline{\mathbf{Y}}) = \frac{\partial \psi}{\partial \underline{\mathbf{Y}}} = \frac{\mathrm{d}\Psi}{\mathrm{d}\underline{\mathbf{Y}}} = \triangledown \Psi(\underline{\mathbf{Y}}). \tag{33}$$

A.2 Isotropy

A material is isotropic if and only if, for any proper orthogonal second-order tensor $\mathbf{Q}$

$$\underline{\mathbf{T}}(\underline{\mathbf{Y}}\mathbf{Q}) \langle \boldsymbol{\xi} \rangle = \underline{\mathbf{T}}(\underline{\mathbf{Y}}) \langle \mathbf{Q}\boldsymbol{\xi} \rangle . \tag{34}$$

Physically, Eq. (34) reflects the fact that the force state is invariant by applying rotations before deformations.

A.3 Isotropic elastic solid

Let ϑ be a non-local volume dilatation [Silling and Lehoucq, 2010, Le et al., 2014, Sarego et al., 2016, Le and Bobaru, 2017] such as

$$\vartheta(\underline{e}) = \frac{\varrho}{q} (\underline{w}\, \underline{x}) \bullet \underline{e} \tag{35}$$

$\underline{w}$ is the *scalar influence state* used to weight the bonds influence on the force state calculation and $\underline{x} = |\underline{\mathbf{X}} \langle \boldsymbol{\xi} \rangle| = \|\boldsymbol{\xi}\|_2$. q is the *weighted volume* such as

$$q = (\underline{w}\, \underline{x}) \bullet \underline{x} \tag{36}$$

$$\varrho = \begin{cases} 3 & \text{in 3D} \\ 2\left(\dfrac{2\nu - 1}{\nu - 1}\right) & \text{in 2D plane stress} \\ 2 & \text{in 2D plane strain} \end{cases} \tag{37}$$

ν is the Poisson's ratio. Finally, $\underline{e}$ is the *scalar extension state* defined by

$$\underline{e} = |\underline{\mathbf{Y}} \langle \boldsymbol{\xi} \rangle| - \underline{x} = \underline{y} - \underline{x}. \tag{38}$$

The *scalar extension state* can be divided into a *spherical part* $\underline{e}^s$ and a *deviatoric part* $\underline{e}^d$ such as

$$\underline{e} = \underline{e}^s + \underline{e}^d = \frac{\underline{x}}{3} \vartheta(\underline{e}) + \underline{e}^d. \tag{39}$$

The *spherical part* represents the isotropic expansion while the *deviatoric part* depicts shear deformations.

Suppose an isotropic elastic material defined by its strain energy density Ψ

$$\Psi(\underline{e}) = \frac{1}{2}\,\alpha^s\,(\underline{w}\,\underline{e}^s) \bullet \underline{e}^s \;+\; \frac{1}{2}\,\alpha^d\,(\underline{w}\,\underline{e}^d) \bullet \underline{e}^d \tag{40}$$

where α^s and α^d are the PD paremeters [Delorme et al., 2017]. They are calibrated to the classical isotropic elastic material properties (K and G, the bulk and shear modulus) by equating the PD strain energy density Ψ to the classical strain energy density for an arbitrary homogeneous deformation under the infinitesimal strain theory [Silling et al., 2007]. One finds [Le et al., 2014,Sarego et al., 2016,Le and Bobaru, 2017,Delorme et al., 2017] that the PD parameters are:

$$\alpha^s = \begin{cases} \dfrac{1}{q}\,(9K) & \text{in 3D} \\ \dfrac{1}{q}\left[9K + G\left(\dfrac{\nu+1}{2\nu-1}\right)^2\right] & \text{in 2D plane stress} \\ \dfrac{1}{q}\,(9K+G) & \text{in 2D plane strain} \end{cases} \tag{41}$$

$$\alpha^d = \begin{cases} \dfrac{1}{q}\,(15G) & \text{in 3D} \\ \dfrac{1}{q}\,(8G) & \text{in 2D plane stress or plane strain} \end{cases} \tag{42}$$

The calibration above also assumes that the material points have a complete neighborhood of size 2δ (*i.e.* $\mathcal{H} = \mathcal{H}_{\boldsymbol{x}}$) filled with the same material. This assumption is not verified within a distance of δ next to a free surface or an interface with another materials and implies that Eqs. (41) and (42) are no more valid near boundaries. A corrective approach, called *force normalization*, was devised to account for that phenomenon [Macek and Silling, 2007].

From Eqs. (38), (35), (39) and (40), one obtains:

$$\Delta\underline{e} = \Delta\underline{e}^s + \Delta\underline{e}^d \tag{43a}$$

$$\Delta\vartheta(\underline{e}) = \frac{\varrho}{q}\,(\underline{w}\,\underline{x}) \bullet \Delta\underline{e} + o(||\Delta\underline{e}||) \tag{43b}$$

$$\Delta\underline{e}^s(\underline{e}) = \frac{x}{3}\,\frac{\varrho}{q}\,(\underline{w}\,\underline{x}) \bullet \Delta\underline{e} + o(||\Delta\underline{e}||) \tag{43c}$$

$$\Delta\underline{e}^d(\underline{e}) = \left[1 - \frac{x}{3}\,\frac{\varrho}{q}\,(\underline{w}\,\underline{x})\right] \bullet \Delta\underline{e} + o(||\Delta\underline{e}||) \tag{43d}$$

$$\Delta\Psi(\underline{e}) = \alpha^s\,(\underline{w}\,\underline{e}^s) \bullet \Delta\underline{e}^s + \alpha^d\,(\underline{w}\,\underline{e}^d) \bullet \Delta\underline{e}^d + o(||\Delta\underline{e}||) \tag{43e}$$

where Δ represents an increment of the function of state resulting from an incremental change to the scalar extension state $\Delta\underline{e}$. This incremental change to the scalar extension state is related to the incremental change to the deformation state $\Delta\underline{\mathbf{Y}}$ as follows

$$\Delta\underline{e} = \frac{\underline{\mathbf{Y}}}{|\underline{\mathbf{Y}}|}\,\Delta\underline{\mathbf{Y}} + o(\|\Delta\underline{\mathbf{Y}}\|) = \underline{\mathbf{M}}\,\Delta\underline{\mathbf{Y}} + o(\|\Delta\underline{\mathbf{Y}}\|). \tag{44}$$

Thus, combining Eqs (38), (33), (43) and (44) leads to the constitutive model of an isotropic elastic material given by the force state

$$\underline{\mathbf{T}}(\underline{\mathbf{Y}}) = \left\{\frac{1}{3}\left(\varrho\alpha^s - (3-\varrho)\alpha^d\right)\underline{w}\,\underline{e}^s + \alpha^d\,\underline{w}\,\underline{e}^d\right\}\underline{\mathbf{M}}. \tag{45}$$

Eq. (45) shows that the constitutive model of an isotropic elastic material corresponds to an ordinary material since $\underline{\mathbf{T}} = \underline{t}\,\underline{\mathbf{M}}$.

References

[Agwai et al., 2010] Agwai, A., Guven, I., and Madenci, E. (2010). Predicting crack initiation and propagation using xfem, czm and peridynamics: A comparative study. In *Electronic Components and Technology Conference (ECTC), 2010 Proceedings 60th*, pages 1178–1185. IEEE, https://doi.org/10.1016/10.1109/ECTC.2010.5490851.

[Avril et al., 2008] Avril, S., Bonnet, M., Bretelle, A.-S., Grédiac, M., Hild, F., Ienny, P., Latourte, F., Lemosse, D., Pagano, S., Pagnacco, E., et al. (2008). Overview of identification methods of mechanical parameters based on full-field measurements. *Experimental Mechanics*, 48(4):381, https://doi.org/10.1007/s11340-008-9148-y.

[Avril et al., 2004] Avril, S., Grédiac, M., and Pierron, F. (2004). Sensitivity of the virtual fields method to noisy data. *Computational Mechanics*, 34(6):439–452, https://doi.org/10.1007/s00466-004-0589-6.

[Avril and Pierron, 2007] Avril, S. and Pierron, F. (2007). General framework for the identification of constitutive parameters from full-field measurements in linear elasticity. *International Journal of Solids and Structures*, 44(14):4978–5002, https://doi.org/10.1016/j.ijsolstr.2006.12.018.

[Belhabib et al., 2008] Belhabib, S., Haddadi, H., Gaspérini, M., and Vacher, P. (2008). Heterogeneous tensile test on elastoplastic metallic sheets: Comparison between fem simulations and full-field strain measurements. *International Journal of Mechanical Sciences*, 50(1):14–21, https://doi.org/10.1016/j.ijmecsci.2007.05.009.

[Bobaru et al., 2016] Bobaru, F., Foster, J. T., Geubelle, P. H., and Silling, S. A. (2016). *Handbook of peridynamic modeling*. CRC Press.

[Bobaru and Hu, 2012] Bobaru, F. and Hu, W. (2012). The meaning, selection, and use of the peridynamic horizon and its relation to crack branching in brittle materials. *International journal of fracture*, 176(2):215–222, https://doi.org/10.1007/s10704-012-9725-z.

[Bobaru et al., 2009] Bobaru, F., Yang, M., Alves, L. F., Silling, S. A., Askari, E., and Xu, J. (2009). Convergence, adaptive refinement, and scaling in 1d peridynamics. *International Journal for Numerical Methods in Engineering*, 77(6):852–877, https://doi.org/10.1002/nme.2439.

[Chen and Gunzburger, 2011] Chen, X. and Gunzburger, M. (2011). Continuous and discontinuous finite element methods for a peridynamics model of mechanics. *Computer Methods in Applied Mechanics and Engineering*, 200(9):1237–1250, https://doi.org/10.1016/j.cma.2010.10.014.

[Claire et al., 2004] Claire, D., Hild, F., and Roux, S. (2004). A finite element formulation to identify damage fields: the equilibrium gap method. *International journal for numerical methods in engineering*, 61(2):189–208, https://doi.org/10.1002/nme.1057.

[Cottin et al., 1984] Cottin, N., Felgenhauer, H.-P., and Natke, H. (1984). On the parameter identification of elastomechanical systems using input and output residuals. *Ingenieur-Archiv*, 54(5):378–387, https://doi.org/10.1007/BF00532820.

[Delorme, 2018a] Delorme, R. (2018a). 3pt_bending_schema. Figshare, https://doi.org/10.6084/m9.figshare.5856717.

[Delorme, 2018b] Delorme, R. (2018b). missing_nodes_schema. Figshare, https://doi.org/10.6084/m9.figshare.7263965.

[Delorme, 2018c] Delorme, R. (2018c). pd_deformation_state_schema. Figshare, https://doi.org/10.6084/m9.figshare.5856888.

[Delorme, 2018d] Delorme, R. (2018d). pd_emu_nd_schema. Figshare, https://doi.org/10.6084/m9.figshare.5856891.

[Delorme, 2018e] Delorme, R. (2018e). pd_inyeractions_schema. Figshare, https://doi.org/10.6084/m9.figshare.5856885.

[Delorme, 2018f] Delorme, R. (2018f). vfm_3pt_bending_schema. Figshare, https://doi.org/10.6084/m9.figshare.5856894.

[Delorme and Diehl, 2018] Delorme, R. and Diehl, P. (2018). Peripyvfm v0.1. https://doi.org/10.5281/zenodo.1462056.

[Delorme et al., 2018] Delorme, R., Diehl, P., and Tabiai, I. (2018). Peripydic v0.1. https://doi.org/10.5281/zenodo.1405731.

[Delorme et al., 2017] Delorme, R., Tabiai, I., Lebel, L. L., and Lévesque, M. (2017). Generalization of the ordinary state-based peridynamic model for isotropic linear viscoelasticity. *Mechanics of Time-Dependent Materials*, 21(4):1–27, https://doi.org/10.1007/s11043-017-9342-3.

[Diehl et al., 2016] Diehl, P., Franzelin, F., Pflüger, D., and Ganzenmüller, G. C. (2016). Bond-based peridynamics: a quantitative study of mode i crack opening. *International Journal of Fracture*, 201(2):157–170, https://doi.org/10.1007/s10704-016-0119-5.

[Du, 2016] Du, Q. (2016). Local limits and asymptotically compatible discretizations. *Handbook of Peridynamic Modeling*, page 87.

[Du and Tian, 2015] Du, Q. and Tian, X. (2015). Robust discretization of nonlocal models related to peridynamics. In *Meshfree Methods for Partial Differential Equations VII*, pages 97–113. Springer, https://doi.org/10.1007/978-3-319-06898-5_6.

[Emmrich and Weckner, 2007] Emmrich, E. and Weckner, O. (2007). The peridynamic equation and its spatial discretisation. *Mathematical Modelling and Analysis*, 12(1):17–27, https://doi.org/10.3846/1392-6292.2007.12.17-27.

[Florentin and Lubineau, 2010] Florentin, E. and Lubineau, G. (2010). Identification of the parameters of an elastic material model using the constitutive equation gap method. *Computational Mechanics*, 46(4):521–531, https://doi.org/10.1007/s00466-010-0496-y.

[Foster et al., 2011] Foster, J. T., Silling, S. A., and Chen, W. (2011). An energy based failure criterion for use with peridynamic states. *International Journal for Multiscale Computational Engineering*, 9(6), https://doi.org/10.1615/IntJMultCompEng.2011002407.

[Giraudeau and Pierron, 2005] Giraudeau, A. and Pierron, F. (2005). Identification of stiffness and damping properties of thin isotropic vibrating plates using the virtual fields method: theory and simulations. *Journal of Sound and Vibration*, 284(3):757–781, https://doi.org/10.1016/j.jsv.2004.07.009.

[Grédiac, 1989] Grédiac, M. (1989). Principe des travaux virtuels et identification. *Comptes rendus de l'Académie des sciences. Série 2, Mécanique, Physique, Chimie, Sciences de l'univers, Sciences de la Terre*, 309(1):1–5.

[Grédiac et al., 1999] Grédiac, M., Pierron, F., and Surrel, Y. (1999). Novel procedure for complete in-plane composite characterization using a single t-shaped specimen. *Experimental Mechanics*, 39(2):142–149, https://doi.org/10.1007/BF02331118.

[Grédiac et al., 2002a] Grédiac, M., Toussaint, E., and Pierron, F. (2002a). Special virtual fields for the direct determination of material parameters with the virtual fields method. 1 – Principle and definition. *International Journal of Solids and Structures*, 39(10):2691–2705, https://doi.org/10.1016/S0020-7683(02)00127-0.

[Grédiac et al., 2002b] Grédiac, M., Toussaint, E., and Pierron, F. (2002b). Special virtual fields for the direct determination of material parameters with the virtual fields method. 2 – Application to in-plane properties. *International Journal of Solids and Structures*, 39(10):2707–2730, https://doi.org/10.1016/S0020-7683(02)00128-2.

[Grédiac et al., 2003] Grédiac, M., Toussaint, E., and Pierron, F. (2003). Special virtual fields for the direct determination of material parameters with the virtual fields method. 3. application to the bending rigidities of anisotropic plates. *International Journal of Solids and Structures*, 40(10):2401–2419, https://doi.org/10.1016/S0020-7683(03)00030-1.

[Hu et al., 2015] Hu, Y., De Carvalho, N., and Madenci, E. (2015). Peridynamic modeling of delamination growth in composite laminates. *Composite Structures*, 132:610–620, https://doi.org/10.1016/j.compstruct.2015.05.079.

[Kramer and Scherzinger, 2014] Kramer, S. L. and Scherzinger, W. M. (2014). Implementation and evaluation of the virtual fields method: Determining constitutive model parameters from full-field deformation data. Technical Report SAND2014-17871, Sandia National Laboratories.

[Ladeveze and LeDantec, 1992] Ladeveze, P. and LeDantec, E. (1992). Damage modelling of the elementary ply for laminated composites. *Composites science and technology*, 43(3):257–267, https://doi.org/10.1016/0266-3538(92)90097-M.

[Le and Bobaru, 2017] Le, Q. and Bobaru, F. (2017). Surface corrections for peridynamic models in elasticity and fracture. *Computational Mechanics*, pages 1–20, https://doi.org/10.1007/s00466-017-1469-1.

[Le et al., 2014] Le, Q., Chan, W., and Schwartz, J. (2014). A two-dimensional ordinary, state-based peridynamic model for linearly elastic solids. *International Journal for Numerical Methods in Engineering*, 98(8):547–561, https://doi.org/10.1002/nme.4642.

[Le Digabel, 2011] Le Digabel, S. (2011). Algorithm 909: NOMAD: Nonlinear Optimization with the MADS algorithm. *ACM Transactions on Mathematical Software*, 37(4):44:1–44:15, https://doi.org/10.1145/1916461.1916468.

[Lecompte et al., 2007] Lecompte, D., Smits, A., Sol, H., Vantomme, J., and Van Hemelrijck, D. (2007). Mixed numerical-experimental technique for orthotropic parameter identification using biaxial tensile tests on cruciform specimens. *International Journal of Solids and Structures*, 44(5):1643–1656, https://doi.org/10.1016/j.ijsolstr.2006.06.050.

[Littlewood, 2015] Littlewood, D. J. (2015). Roadmap for peridynamic software implementation. Technical Report SAND2015-9013, Sandia National Laboratories.

[Macek and Silling, 2007] Macek, R. W. and Silling, S. A. (2007). Peridynamics via finite element analysis. *Finite Elements in Analysis and Design*, 43(15):1169–1178, https://doi.org/10.1016/j.finel.2007.08.012.

[Parks et al., 2008] Parks, M. L., Lehoucq, R. B., Plimpton, S. J., and Silling, S. A. (2008). Implementing peridynamics within a molecular dynamics code. *Computer Physics Communications*, 179(11):777–783, https://doi.org/10.1016/j.cpc.2008.06.011.

[Pierron and Grédiac, 2012] Pierron, F. and Grédiac, M. (2012). *The virtual fields method: extracting constitutive mechanical parameters from full-field deformation measurements*. Springer Science & Business Media, https://doi.org/10.1007/978-1-4614-1824-5.

[Rouger et al., 1991] Rouger, F., Khebibeche, M., and Le Govic, C. (1991). Non determined tests as a way to identify wood elastic parameters the finite element approach. In *Mechanical Identification of Composites*, pages 82–90. Springer, https://doi.org/10.1007/978-94-011-3658-7_8.

[Sarego et al., 2016] Sarego, G., Le, Q. V., Bobaru, F., Zaccariotto, M., and Galvanetto, U. (2016). Linearized state-based peridynamics for 2-d problems. *International Journal for Numerical Methods in Engineering*, 108(10):1174–1197, https://doi.org/10.1002/nme.5250.

[Seleson, 2014] Seleson, P. (2014). Improved one-point quadrature algorithms for two-dimensional peridynamic models based on analytical calculations. *Computer Methods in Applied Mechanics and Engineering*, 282:184–217, https://doi.org/10.1016/j.cma.2014.06.016.

[Silling, 2000] Silling, S. A. (2000). Reformulation of elasticity theory for discontinuities and long-range forces. *Journal of the Mechanics and Physics of Solids*, 48(1):175–209, https://doi.org/10.1016/S0022-5096(99)00029-0.

[Silling, 2016] Silling, S. A. (2016). Handbook of peridynamic modeling. In [Bobaru et al., 2016], chapter Why Peridynamics?, pages 3–23.

[Silling and Askari, 2005] Silling, S. A. and Askari, E. (2005). A meshfree method based on the peridynamic model of solid mechanics. *Computers & structures*, 83(17):1526–1535, https://doi.org/10.1016/j.compstruc.2004.11.026.

[Silling et al., 2007] Silling, S. A., Epton, M., Weckner, O., Xu, J., and Askari, E. (2007). Peridynamic states and constitutive modeling. *Journal of Elasticity*, 88(2):151–184, https://doi.org/10.1007/s10659-007-9125-1.

[Silling and Lehoucq, 2008] Silling, S. A. and Lehoucq, R. B. (2008). Convergence of peridynamics to classical elasticity theory. *Journal of Elasticity*, 93(1):13–37, https://doi.org/10.1007/s10659-008-9163-3.

[Silling and Lehoucq, 2010] Silling, S. A. and Lehoucq, R. B. (2010). Peridynamic theory of solid mechanics. *Advances in Applied Mechanics*, 44(1):73–166, https://doi.org/10.1016/S0065-2156(10)44002-8.

[Sutton et al., 2009] Sutton, M. A., Orteu, J. J., and Schreier, H. (2009). *Image correlation for shape, motion and deformation measurements: basic concepts, theory and applications*. Springer Science & Business Media, https://doi.org/10.1007/978-0-387-78747-3.

[Tian and Du, 2013] Tian, X. and Du, Q. (2013). Analysis and comparison of different approximations to nonlocal diffusion and linear peridynamic equations. *SIAM Journal on Numerical Analysis*, 51(6):3458–3482, https://doi.org/10.1137/13091631X.

[Toussaint et al., 2006] Toussaint, E., Grédiac, M., and Pierron, F. (2006). The virtual fields method with piecewise virtual fields. *International Journal of Mechanical Sciences*, 48(3):256–264, https://doi.org/10.1016/j.ijmecsci.2005.10.002.

[Turner, 2014] Turner, D. (2014). Peridynamics-based digital image correlation algorithm suitable for cracks and other discontinuities. *Journal of Engineering Mechanics*, 141(2):04014115, https://doi.org/10.1061/(ASCE)EM.1943-7889.0000831.

[Turner et al., 2015] Turner, D., van Bloemen Waanders, B., and Parks, M. (2015). Inverse problems in heterogeneous and fractured media using peridynamics. *Journal of Mechanics of Materials and Structures*, 10(5):573–590, https://doi.org/10.2140/jomms.2015.10.573.

[Weckner and Emmrich, 2005] Weckner, O. and Emmrich, E. (2005). Numerical simulation of the dynamics of a nonlocal, inhomogeneous, infinite bar. *Journal of Computational and Applied Mechanics*, 6(2):311–319.